Available online at www.sciencedirect.com
ScienceDirect
Journal of Nuclear Materials 360 (2007) 186–195
journal of nuclear materials
www.elsevier.com/locate/jnucmat

Welding-induced microstructure in austenitic stainless steels before and after neutron irradiation

R. Stoenescu [a,b,*], R. Schäublin [a], D. Gavillet [b], N. Baluc [a]

[a] Fusion Technology Materials, CRPP – EPFL, Association EURATOM – Confederation Suisse, 5232 Villigen PSI, Switzerland
[b] Laboratory for Materials Behaviour, Paul Scherrer Institute, 5232 Villigen PSI, Switzerland

Received 16 December 2005

Abstract

The effects of neutron irradiation on the microstructure of welded joints made of austenitic stainless steels have been investigated. The materials were welded AISI 304 and AISI 347, so-called test weld materials, and irradiated with neutrons at 300 °C to 0.3 and 1.0 dpa. In addition, an AISI 304 type from a decommissioned pressurised water reactor, so-called in-service material, which had accumulated a maximum dose of 0.35 dpa at about 300 °C, was investigated. The microstructure of heat-affected zones and base materials was analysed before and after irradiation, using transmission electron microscopy. Neutron diffraction was performed for internal stress measurements. It was found that the heat-affected zone contains, relative to the base material, a higher dislocation density, which relates well to a higher residual stress level and, after irradiation, a higher irradiation-induced defect density. In both materials, the irradiation-induced defects are of the same type, consisting in black dots and Frank dislocation loops. Careful analysis of the irradiation-induced defect contrast was performed and it is explained why no stacking fault tetrahedra could be identified.

1. Introduction

Welded austenitic stainless steels are commonly used for the fabrication of internal components of light water reactors, such as core shrouds. The core shrouds of nuclear reactors are subjected to radiation, heat, as the operating temperature is 288 °C, stresses and corrosive environments. It is well known that the failure of the welded reactor components, typically made of AISI 304, AISI 304L, and/or AISI 347 types of austenitic stainless steels, usually occurs close to the welds. Examinations of core shrouds have revealed the presence of circumferential cracks in the heat-affected zone (HAZ) induced by the welding process [1,2]. The HAZ is defined as the region adjacent to the weld metal, which is subjected to heating during the welding process. Although the behaviour of austenitic stainless steels as base material (BM) has been thoroughly investigated, studies of weld metal and HAZ are scarce.

The behaviour of a welded joint is required to be the same as the BMs it joints together. In practice this objective is not always achieved because the welding process itself introduces secondary phases,

* Corresponding author. Present address: Institutt for Energiteknikk/OECD Halden Reactor Project, P.O. Box 173, N-1751 Halden, Norway. Tel.: +47 69 21 2357; fax: +47 69 21 2201.
E-mail address: ralucas@hrp.no (R. Stoenescu).

0022-3115/$ - see front matter
doi:10.1016/j.jnucmat.2006.10.007

residual stresses, defects and phase transformations which can degrade the properties of the welded joints as compared to the BM [3,4]. In fusion welding, a region of the HAZ is heated within the carbide precipitation temperature range, so that intergranular carbide precipitation can occur [5]. As a consequence of welding, the grains are enriched in chromium and depleted in nickel [6].

Although the specific damage microstructure depends on the particularities of the stainless steel type and on the irradiation conditions, typical irradiation-induced microstructural features in austenitic stainless steels consist in the so-called 'black dots' for the unidentified nanometric defects, Frank dislocation loops, cavities [7–13] and, according to some authors, stacking fault tetrahedra (SFT) [14–17]. Irradiation induces depletion in chromium, manganese and molybdenum at the grain boundaries and enrichment in nickel and silicon [18,19]. Irradiation can also lead to localised stress relaxation.

The goal of this study is to better understand the effects of neutron irradiation on the microstructure of HAZs of three types of austenitic stainless steels.

2. Experimental

Two sets of materials were used in the present study. The first set was composed of two types of austenitic stainless steels, AISI 304 and AISI 347, so-called test weld materials, with the chemical composition listed in Table 1. Two plates of each material were welded together by Framatome ANP, Germany [20]. The chosen fusion welding procedure was a compromise between the conditions applied to real boiling water reactors (BWR) components and the restrictions imposed by the analysis tools used in this research project. Optical microscopy observations performed on the materials after welding have revealed that the grain size presents a significant variation as a function of the distance from the fusion line (FL). It appears much higher in the HAZ, about 60–65 μm, with respect to the BM (40–50 μm). No significant difference is observed between the grain sizes of the two materials. The width of the HAZ is approximately 600 μm in both materials. The approximation of the width of the HAZ allowed to further prepare specimens for irradiation and microscopy observations.

After welding, specimens for microscopy observations were cut along the FL, in the HAZ, and irradiated in the High Flux Reactor in NRG, Petten, the Netherlands. The irradiation temperature was 290 °C, with a maximum target deviation of ±10 °C. Two doses were accumulated, namely 0.3 and 1.0 dpa, for both AISI 304 and AISI 347.

The other set of materials, so-called in-service material, refers to the thermal shield of a decommissioned experimental pressurised water reactor (PWR), the BR-3, in Mol, Belgium. The operating temperature and power of this reactor were lower than those of the new generation of PWRs. Therefore, the exposure conditions of the thermal shield material are comparable to the current exposure conditions in BWRs, where the coolant temperature is about 290 °C, whereas it is 320 °C and higher in the new PWRs [20]. The thermal shield was made of the welded austenitic stainless steel BR 304, with the chemical composition listed in Table 1. Two plates, having the same thermal history, were selected. One plate (Block A), referred to as the reference material or unirradiated material, was taken from the top of the thermal shield. The other plate (Block B) was taken at 23 mm above the mid plane, in the high neutron flux region. The accumulated dose of the in-service material decreases from the inner side of the reactor to the outer side, due to self-shielding, reaching values between 1.3×10^{-4} and 1.3×10^{-5} dpa for Block A and between 0.35 and 0.12 dpa for Block B [20]. Optical microscopy observations revealed an increase in the grain size close to the FL (151 μm) as compared to the values far away from the FL (106.8 μm), for both Block A and Block B materials.

The residual stresses induced by the welding process in the unirradiated materials have been determined by neutron diffraction, using the POLDI (Pulse Over-Lap Diffraction) facility at the Paul

Table 1
Chemical composition of the materials, in wt%

Material	C	Si	Mn	P	S	Cr	Ni	Nb	Fe
AISI347	0.03	0.46	1.22	0.034	0.005	17.69	10.34	0.49	Bal.
AISI304	0.042	0.31	1.63	0.03	0.01	18.36	9.5	–	Bal.
BR304	0.08	0.75	2	0.045	0.03	18.0	8.0	–	Bal.

Scherrer Institute, Switzerland. The principle of this method is described in [21,22].

The evolution of the microstructure has been studied by performing transmission electron microscopy (TEM) of samples cut out along the FL, at varying distances from the FL and on samples from the BM, for all materials and all accumulated doses. A micrograph of the weld metal and TEM samples positions is shown in Fig. 1. TEM observations were performed using a JEOL 2010 microscope, operating at 200 kV, equipped with a detector for chemical analysis by X-ray energy dispersive spectrometry (EDS).

Because of the high activity of some specimens, besides 3 mm TEM disks, 1 mm TEM disks were also used. The specimens were electrolytically thinned by jet polishing at 0 °C and at about 13.5 V, in a solution of 10% perchloric acid, 15% ethylene glycol and 75% methanol.

The overview of the microstructure was obtained by conventional bright-field and dark-field imaging techniques. The small irradiation-induced defects were studied using dark-field and weak-beam dark-field imaging techniques [23]. The convergent beam electron diffraction (CBED) technique was applied for thickness measurements and for precise lattice parameter identification. The dislocation density in the unirradiated materials was determined from bright-field TEM images at different distances from the FL. The defect size distribution of irradiation-induced defects was determined using series of micrographs imaged under different dark-field and weak-beam conditions. The error in determination of loop number densities is calculated as a sum of factors [24] taking into account the statistical error, calculated as: $E = T^{-1/2}$, where T is the total number of defects counted for one condition. In addition, the error in determination of foil thickness was considered. The foil thickness has been determined using the spacing between the Kossel–Möllenstedt lines in CBED mode. The uncertainty in the foil thickness using CBED is estimated to be ±10% [25]. Another error comes from the proportion of loops which can be seen in TEM because of the extinction arising for the loops for which $\vec{g} \cdot \vec{d} = 0$ [26], where **g** is the diffraction vector and **b** is the Burgers vector. Different diffraction conditions are used in order to avoid this extinction and the appropriate correction factor is applied [24].

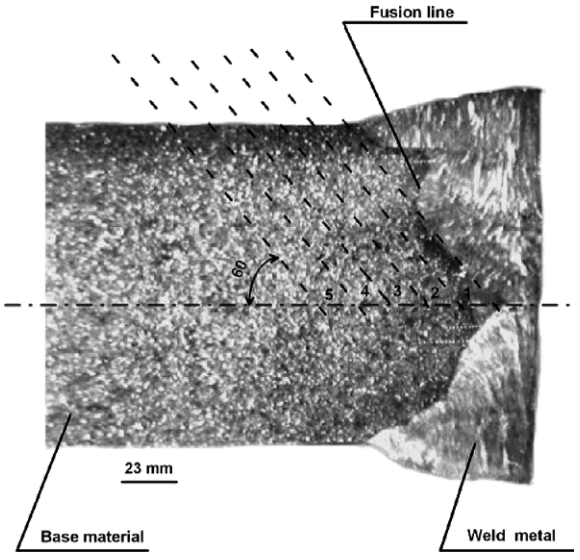

Fig. 1. Micrograph of the weld metal and schematic of sample preparation from the HAZ. Specimens were cut along the FL, according to the dashed lines, with an angle of 60° corresponding to the weld edge preparation.

3. Results and discussion

3.1. Residual stress measurements

The residual stresses induced by the welding process have been measured on the unirradiated test weld materials using a neutron diffraction technique [21,22]. The residual stresses measured for example in the AISI 304 are plotted in Fig. 2. They mainly concentrate in the longitudinal direction, reaching the highest values in the centre of the weld. The residual stresses are correlated with the microstructure observations.

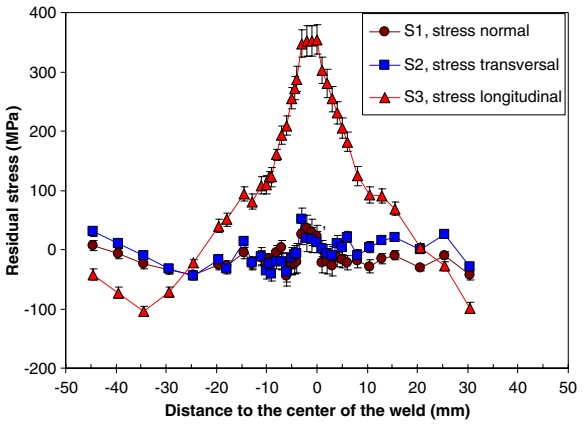

Fig. 2. Residual stresses variations along a line perpendicular to the weld in the unirradiated AISI 304.

3.2. Microstructure of the unirradiated test weld materials

A bright-field image of the AISI 347 BM, unaffected by the thermal cycles upon welding, is presented in Fig. 3. The microstructure is typical of that of austenitic stainless steels, with isolated dislocations and extended stacking faults. Fig. 4 shows a bright field image of the AISI 347 HAZ. Close to the FL one observes recrystallised areas, relatively free of dislocations, surrounded by a matrix with a higher dislocation density than in the BM. No differences were observed between AISI 304 and AISI 347 regarding the microstructural features present in the BM and in the HAZ. It is known that, under welding, austenitic stainless steels develop a duplex microstructure composed of ferrite and austenite grains [27–29]. In this case, the ferrite is present as an interphase that could be located in thin sheets surrounding austenite grains. It appears in TEM as islands with dimensions between 2 and 12 μm. The amount of ferrite in the HAZ of both AISI 304 and AISI 347 was determined from TEM images from surface fraction to be about 3 vol.% in the austenitic matrix. To authenticate the ferritic structure, the interphase was further studied by TEM using selected area diffraction (SAD) and CBED. In the case of AISI 347, the lattice parameter of the austenitic matrix was determined from SAD images to be (0.359 ± 0.014) nm, while for the ferrite it was found to be (0.304 ± 0.014) nm.

To further analyse the interphase, the CBED patterns of the matrix and interphase were indexed and compared. Fig. 5 shows a CBED of the (1 1 1) zone axis of the matrix, together with the corresponding SAD, typical of an fcc structure. The CBED pattern of the (1 1 1) zone axis in the interphase is presented in Fig. 6, with the corresponding SAD. These patterns are characteristic of a bcc structure, demonstrating the ferritic nature of the interphase. Kikuchi patterns were simulated using the jEMS software [30] to better determine the lattice parameter. Fig. 7 shows a simulated Kikuchi pattern superimposed on an experimental CDEB image of the matrix, in the case of AISI 347 HAZ. The image simulations were performed for the $(\bar{1}\,\bar{1}\,\bar{1})$ zone axis, the $(\bar{1}\,\bar{1}\,\bar{1})$ foil normal and the centre of Laue circle

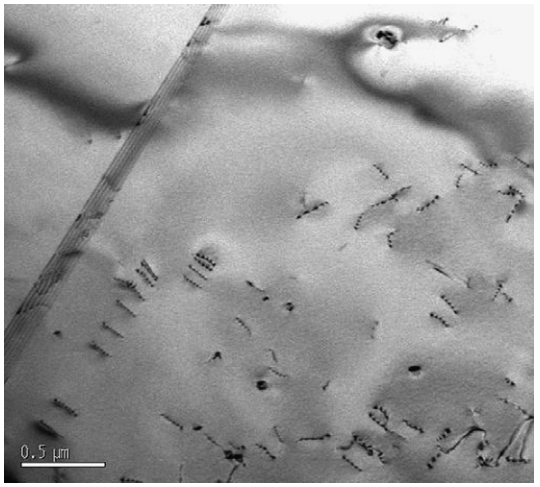

Fig. 3. TEM bright-field image of AISI 347 base material.

Fig. 4. TEM bright-field image of AISI 347 heat affected zone.

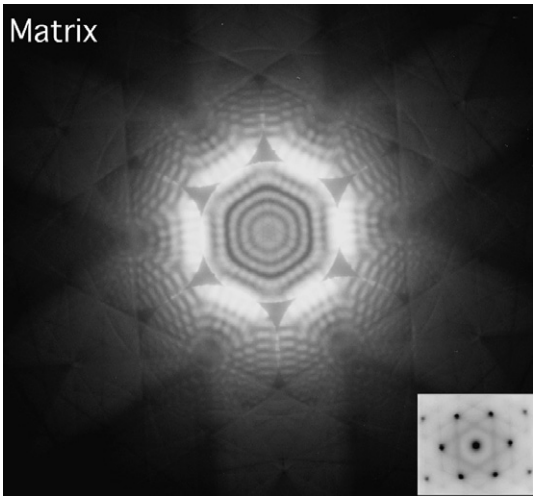

Fig. 5. CBED pattern and corresponding SAD pattern obtained for the (1 1 1) zone axis of the matrix (fcc structure).

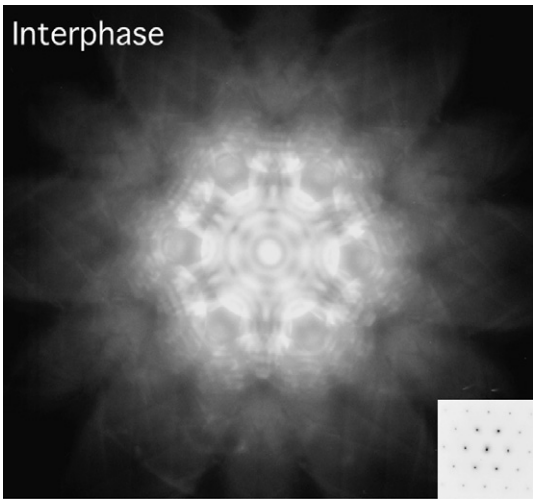

Fig. 6. CBED pattern and corresponding SAD pattern obtained for the (1 1 1) zone axis of the interphase (bcc structure).

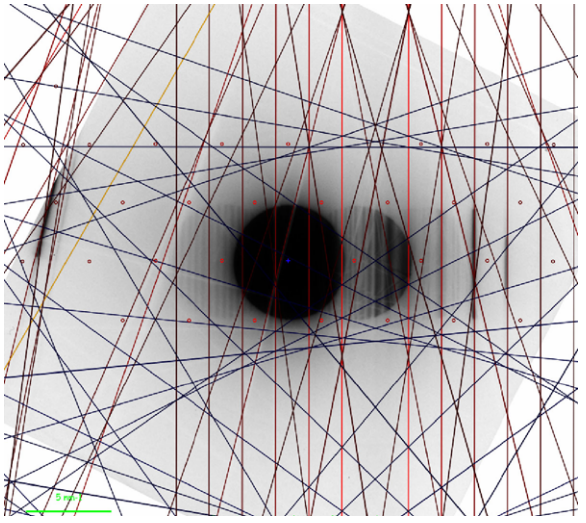

Fig. 7. Simulated Kikuchi pattern for the $(\bar{1}\,\bar{1}\,\bar{1})$ zone axis, the $(\bar{1}\,\bar{1}\,\bar{1})$ foil normal and the centre of Laue circle at (8.8, −15.04, 6.21) superimposed on experimental CBED image of the interphase in the AISI 347 HAZ.

at $(8.8, -15.04, 6.21)$. The lattice parameter of the austenite, determined by fitting the simulated Kikuchi lines to the experimental image, was found to be $a = (0.3677 \pm 0.0010)$ nm.

The chemical composition of the interphase was determined in TEM by EDS and compared to the one obtained for the matrix. The results for AISI 347 are listed in Table 2. It was found that Cr is enriched in the interphase, while Ni is depleted. This is in agreement with the previous conclusion, pointing out that the interphase is of ferrite type, as it is well known that Cr and Si are ferrite forming elements, while Ni and Fe are austenite forming elements [6].

Table 2
Chemical composition of the matrix and the interphase of AISI 347 determined by EDS, in wt%

Position	Si	Cr	Mn	Fe	Ni	Nb
Matrix	1.7	20.6	1.3	67.29	9.02	0.18
Interphase	1.9	29.83	0.7	65.03	4.22	0.08

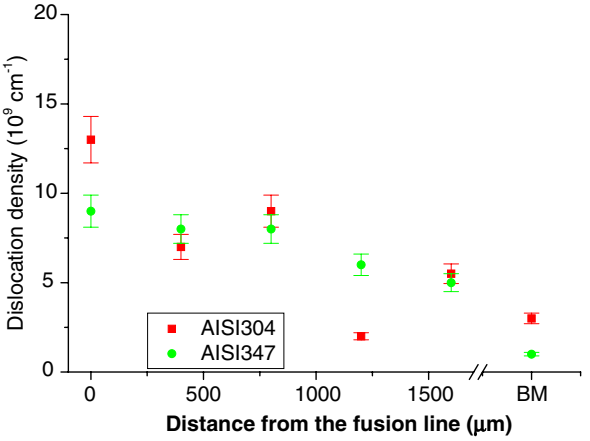

Fig. 8. Dislocation density as a function of the distance from the fusion line for the unirradiated test materials.

The mean dislocation density has been evaluated from TEM images of the BM and HAZ of both unirradiated materials. Results are reported in Fig. 8 as a function of the distance from the FL. The dislocation density decreases as the distance from the FL increases and no significant difference between the two materials is observed. The higher dislocation density in the HAZ as compared to the BM can be explained by the successive heating and cooling processes taking place in the HAZ during the welding process which introduces mechanical stresses in the material. These measurements are in good correlation with the residual stresses, in the sense that the increase in residual stresses corresponds to an increase in dislocation density.

3.3. Microstructure of the irradiated test weld materials

The microstructure of both AISI 304 and AISI 347 after neutron irradiation changes in one

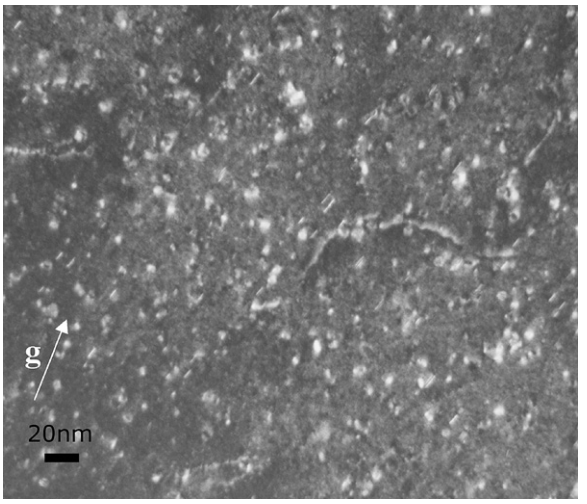

Fig. 9. TEM weak-beam image g(5g), g {200}, close to a zone axis ⟨011⟩ of AISI 347 irradiated up to 1 dpa.

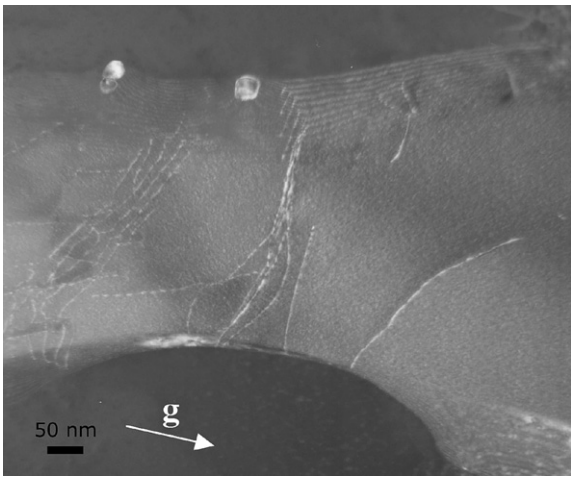

Fig. 10. TEM weak-beam image g(4g), g {111}, close to a zone axis ⟨311⟩ of AISI 304 ferrite interphase irradiated up to 0.3 dpa.

dominated by irradiation-induced defects: black dots and Frank dislocation loops. Fig. 9 shows a weak-beam dark-field image of the austenite matrix of AISI 347 close to the FL, following irradiation to 1.0 dpa. The so-called 'black dots' relate to contrasts in TEM appearing as white dots in weak-beam dark field images and that cannot be related to specific defects. The Frank dislocation loops have been identified on the basis of their specific black/white image contrast, as will be discussed later.

In Fig. 10 a detail of the interphase in AISI 304 HAZ irradiated up to 0.3 dpa is shown, presenting a background free of 'black dots'. Either no defects have been produced by neutron irradiation in the interphase of bcc structure, or the defects are too small to be resolved by conventional TEM. Note that the TEM resolution is about 1 nm in dark-field weak-beam imaging [31]. The absence of TEM observable irradiation-induced defects in the ferrite phase can also be related to the lower defect accumulation rate under irradiation in bcc structures with respect to fcc structures [9].

No significant changes were observed in the irradiation-induced microstructure with varying irradiation dose, in terms of density, size and morphology. The defect density and size distribution of irradiation-induced defects were determined using series of micrographs imaged under different dark field and weak-beam dark field conditions; they are reported in Table 3. The total defect density, including black dots and Frank dislocation loops, shows no significant variation with increasing irradiation dose, while the total defect size is observed to slightly increase with increasing irradiation dose.

For irradiation temperatures below 300 °C it is postulated by some authors that the Frank loops are interstitial in nature, while black dots are predominantly of vacancy nature [32–35]. More recent studies contradict this statement and conclude that Frank loops with sizes in the range of 1–30 nm can be either vacancy or interstitial type [14]. In the present work, the nature of Frank loops has been investigated using the inside–outside contrast method [24]. Weak-beam dark field TEM was used,

Table 3
Defect density and mean size versus dose of the AISI 304 and AISI 347 irradiated materials

Material	Dose [dpa]	Black dots		Dislocation loops		Total density [m^{-3}]
		Density [m^{-3}]	Mean size [nm]	Density [m^{-3}]	Mean size [nm]	
AISI 304	0.3	1.1×10^{23}	2.2	1.6×10^{23}	5.4	2.7×10^{23}
	1.0	1.4×10^{23}	2.2	1.6×10^{23}	5.4	3.0×10^{23}
AISI 347	0.3	5.2×10^{22}	2.2	7.8×10^{22}	5.6	1.3×10^{23}
	1.0	3.0×10^{22}	2.3	7.7×10^{22}	7.7	1.1×10^{23}

as it allows obtaining the best spatial resolution in diffraction contrast. In order to identify the inclination of the habit plane of the loop, a pair of pictures is taken under exactly the same diffraction conditions, defined by the diffraction vector, **g**, and the deviation parameter, but using different sample orientations. Usually a tilt of 10–20° is sufficient. A stereoscopic observation using both pictures allows determining the orientation of the loop habit plane. In essence, it is the evolution of the width of the loop contrast from one picture to the other that allows determining its inclination.

Fig. 11 shows two experimental weak-beam dark-field TEM images taken with a diffraction vector {200}, close to a zone axis ⟨011⟩, under slightly different angles. There is a tilt of about 10° between the two pictures in Fig. 11(a) and (b). The corresponding diffraction vectors are inserted in the upper part of the images. The two upper loops marked with arrows exhibit an outside contrast that is broader in Fig. 11(a) than in Fig. 11(b), but the loop at the bottom of the image exhibits a narrower contrast. It is concluded that the two upper loops are interstitial in nature, while the one at the bottom is made of vacancies. This analysis indicates that Frank loops can be either interstitial or vacancy in nature.

SFTs have been observed in irradiated austenitic stainless steels [16–18], usually in low densities (<1%) and in high purity alloys. However, Dai [15] observed in an irradiated 304 stainless steel a SFT density corresponding to about 20–25% of the total density of defects. In the present study, only a small amount of image contrasts that could stem from SFTs were identified. It should be noted that one faces here the problem of interpretation of TEM images. In austenitic stainless steels triangular-shaped contrasts can appear in TEM pictures as a result of defects overlapping in the electron beam direction. In this view, a careful analysis has been performed in the present study. One example is shown in Fig. 12, where two beam dark-field images of a small irradiation-induced defect in AISI 347 irradiated to 1.0 dpa were taken close to a ⟨110⟩ zone axis. In Fig. 12(a) taken with a diffraction vector of the {200} type, the image contrast presents a triangular aspect. When the diffraction condition is changed to a diffraction vector of the {220} type, the image contrast looses its triangular aspect, indicating that it cannot result from a SFT, as in Fig. 12(b). Typically, when looking down a zone axis of the ⟨011⟩ type, Frank loops lying in {111} planes will appear edge-on for the two families of planes (e.g. $(1\,1\,\bar{1})$ and $(1\,\bar{1}\,1)$) containing the zone axis (e.g. [011]). The image contrast is then a

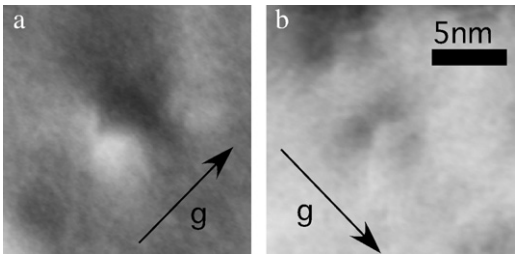

Fig. 12. Strain field contrast of a small irradiation-induced defect imaged in two-beam dark field condition using (a) a {200} reflection and (b) a {220} reflection, close to a ⟨110⟩ zone axis.

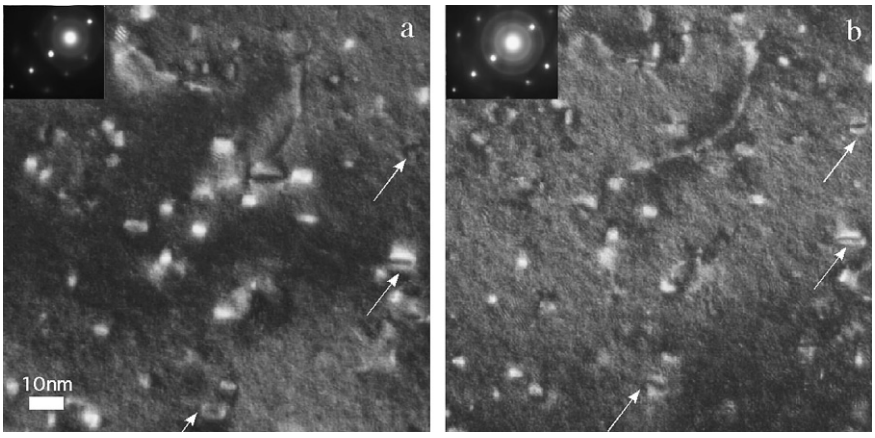

Fig. 11. TEM weak-beam dark field TEM images, g (6g), g {200}, close to ⟨011⟩ zone axis of AISI 347 irradiated to 1 dpa, taken at two different tilt angles.

well delineated straight segment, bounded on each side by a light contrast. When two of these loops are lying in two conjugate {1 1 1} planes containing the zone axis ⟨0 1 1⟩ and are located one above the other, the resulting contrast, actually composed of two straight segments touching each other, may have the appearance of a triangle. The triangular appearance of the contrast could also be due to the asymmetrical strain field of a single defect, whose contrast varies with the diffraction condition, as suggested by Jenkins and Kirk [24].

The low stacking fault energy (SFE) in austenitic stainless steels (between 10 and 50 mJ/m^2 [36]) should favour the formation of SFTs. Solely on the basis of SFE and the shear modulus, by calculating the ratio of the SFE (γ) to the shear modulus (μ) times the Burgers vector (**b**), $\gamma/(\mu\cdot\mathbf{b})$, one may infer that SFTs should be the dominating features in irradiated stainless steels [37]. Considering $\gamma = 38\times10^{-3}$ J/m^2, $\mu = 74.23\times10^{9}$ N/m^2, $\mathbf{b} = 0.253\times10^{-9}$ m [20], the ratio has a value of 1/490 which, according to Schäublin et al. [37] should favour the formation of SFTs, and this is actually not the case. A similar idea was proposed by Zinkle et al. [38,39] who suggested that copper alloys contain a smaller fraction of SFTs than pure copper, even though their SFE is lower than in pure copper.

The scarcity or absence of SFTs in irradiated stainless steels may be rationalised in two ways. One scenario consists in the premature partial dissociation of Frank loops, before they reach the triangular shape needed for the SFT formation, giving the loop a waffle-like structure, as suggested by Jenkins and Kirk [24]. After reaching this shape, the loop morphology cannot evolve anymore so easily, as this would require the constriction of one or more of the dissociated edges in order to allow for the glide of the boarding dislocation to a triangular shape. The small SFE in stainless steels would be in favour of such a premature dissociation. In the other scenario, it is suggested that impurities and alloying elements are altering the evolution of Frank loops towards SFTs. In alloys, due to the different atom sizes, the recoil collision sequences are less efficient than in pure metals, with uniform atom size. This can modify the displacement cascade process, in the sense that the interstitials and vacancies will not be effectively separated from one another and the vacancy-rich core may not develop so well [40]. Vacancies can preferentially migrate to solute atoms, reducing the possibility of SFT formation [33]. In addition, the differences in atomic radii (between the Fe atoms and the other alloying elements) might be sufficient to locally impede the nucleation and/or glide of the 1/6⟨1 1 2⟩ Shockley partial necessary to unfold the stacking fault planes that are the premises of a nascent SFT.

Our investigation of the nature of Frank loops supports this analysis. The fact that Frank loops can be either interstitial or vacancy in nature explains the scarcity of the observed SFTs. The balance of point defects, interstitials and vacancies, produced in even quantities by the impinging particle can be maintained, as vacancies can be equally found in Frank loops, thus voiding the need of SFT, which are intrinsically vacancy in nature.

3.4. Microstructure of the in-service material

The study of the in-service material provided information about the evolution of the microstructure in the HAZ in comparison with the BM.

The in-service material shows the same microscopic features as those in the test weld materials. Weak-beam dark-field TEM images of the low dose and high dose in-service material, far away from the FL, are shown in Figs. 13 and 14, respectively. The low dose in-service material (Block A) exhibits a microstructure typical of austenitic stainless steels, with isolated dislocations and extended stacking faults. No irradiation-induced defects are visible in TEM. When the irradiation dose is increased to

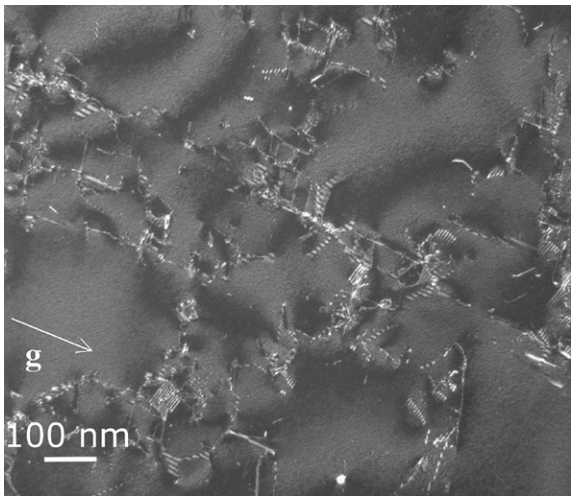

Fig. 13. TEM weak-beam image g (4g), g {2 0 0}, close to a zone axis ⟨0 1 1⟩, of the low dose in-service (Block A) BM (4 mm away from the fusion line) irradiated to 1.3×10^{-5} dpa.

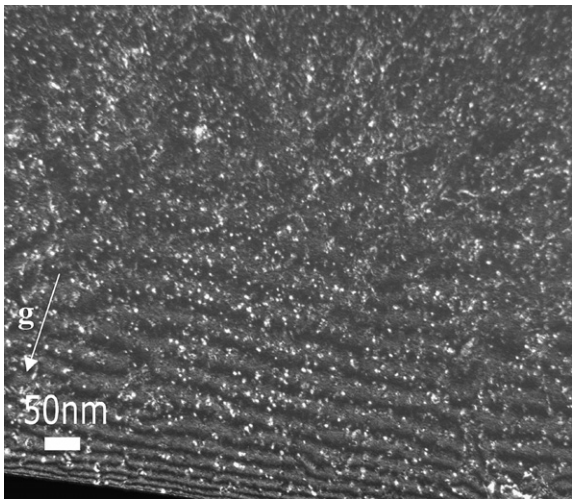

Fig. 14. TEM weak-beam image g (5g), g {200}, close to a zone axis ⟨011⟩, of the high dose in-service (Block B) BM (far away from the fusion line) irradiated to 0.35 dpa.

0.35 dpa, irradiation-induced defects such as black dots and Frank dislocation loops are observed.

The mean dislocation density was determined for both HAZ and BM of the Block A material. The measured values range from $3.9\times10^{10}\,cm^{-2}$ at 1.3×10^{-5} dpa to $4.8\times10^{10}\,cm^{-2}$ at 1.3×10^{-4} dpa for the BM and from $4.6\times10^{10}\,cm^{-2}$ at 1.3×10^{-5} dpa to $7.8\times10^{10}\,cm^{-2}$ at 1.3×10^{-4} dpa in the case of HAZ. There is a small irradiation-induced increase in the dislocation density with dose in both BM and HAZ, the increase being slightly more important in the HAZ. The defect density and size versus dose were determined for the Block B material and they are reported in Table 4. A much higher defect density is observed in the HAZ than in the BM, but the dose dependence is not significant in this dose range.

The higher density of dislocations observed in the HAZ as compared to the BM can be due to the thermal cycles reached during the welding process, which introduce residual stresses in the HAZ.

4. Conclusions

The effects of neutron irradiation on the microstructure of welded joints made of austenitic stainless steels have been investigated. The materials were AISI 304 and AISI 347 welded by fusion welding and irradiated with neutrons at 300 °C to 0.3 and 1.0 dpa. An AISI 304 type austenitic stainless steel from a decommissioned pressurised water reactor (in-service material), which had accumulated a maximum dose of 0.35 dpa at about 300 °C, was also available. Studies of the microstructure of HAZs and BMs have been performed before and after irradiation and the following results were obtained:

- The HAZ is composed of an austenite matrix containing a small amount of ferrite (3 vol.%), resulting from the high temperatures reached during the welding process.
- In the unirradiated test materials (AISI 304 and AISI 347), as well as in the low dose (10^{-4} dpa) in-service material, the dislocation density was found to be higher in the HAZ as compared to the BM, due to the thermal cycles upon welding.
- The residual stress measurements are in good agreement with the microstructure, in the sense that the increase in residual stresses corresponds to an increase in dislocation density.
- Irradiation-induced defects are small black dots which cannot be identified in TEM and Frank dislocation loops which can be either of vacancy or interstitial type. No stacking fault tetrahedra were observed.
- No irradiation-induced defects have been observed by TEM in the bcc ferrite present in the HAZ.
- In the in-service material, the irradiation-induced defect density was found to be higher in the HAZ as compared to the BM, maybe due to the larger grain size in the HAZ as compared to the BM, leaving less sinks, i.e. grain boundaries, for irradiation-induced defects annihilation.

Table 4
Defect density and mean size versus dose of the BM and HAZ of the high dose in-service material

Material	Dose [dpa]	Black dots		Dislocation loops		Total density [m^{-3}]
		Density [m^{-3}]	Mean size [nm]	Density [m^{-3}]	Mean size [nm]	
BM	0.12	9.0×10^{21}	2.0	5.7×10^{21}	5.0	1.5×10^{22}
	0.35	1.7×10^{22}	2.0	6.7×10^{21}	4.0	2.4×10^{22}
HAZ	0.12	6.2×10^{23}	2.5	1.4×10^{23}	5.5	7.6×10^{23}
	0.35	5.2×10^{23}	2.5	2.9×10^{23}	4.5	8.1×10^{23}

- The total defect density seems to increase with the irradiation dose, at least for the in-service material.

Acknowledgments

R. Stoenescu would like to thank Dr Steve Zinkle for fruitful discussions. This work was performed with the financial support of the European Commission, EURATOM FP5, contract number FIKS-CT-2000-00103, INTERWELD.

References

[1] O. Wachter, G. Bruemmer, Nucl. Eng. Des. 168 (1997) 35.
[2] E.A. Kenik, R.H. Jones, G.E.C. Bell, J. Nucl. Mater. 212–215 (1994) 52.
[3] J.W. Elmer, T.A. Palmer, W. Zhang, B. Wood, T. DebRoy, Acta Mater. 51 (2003) 3333.
[4] G. Maussner, L. Scharf, R. Langer, B. Gurovich, Nucl. Eng. Des. 193 (1999) 359.
[5] J.F. Lancaster, Metallurgy of Welding, Abington, Cambridge, 1999.
[6] E. Folkhard, Welding Metallurgy of Stainless Steels, Springer-Verlag, 1984.
[7] S.J. Zinkle, Y. Matsukawa, J. Nucl. Mater. 329–333 (2004) 88.
[8] T.S. Byun, K. Farrell, E.H. Lee, J.D. Hunn, L.K. Mansur, J. Nucl. Mater. 298 (2001) 269.
[9] M. Victoria, N. Baluc, C. Bailat, Y. Dai, M.I. Luppo, R. Schäublin, B.N. Singh, J. Nucl. Mater. 276 (2000) 114.
[10] J. Gan, G.S. Was, J. Nucl. Mater. 297 (2001) 161.
[11] N. Hashimoto, S.J. Zinkle, A.F. Rowcliffe, J.P. Robertson, S. Jitsukawa, J. Nucl. Mater. 283–287 (2000) 528.
[12] N. Yoshida, J. Nucl. Mater. 174 (1990) 220.
[13] D.J. Edwards, E.P. Simonen, F.A. Garner, L.R. Greenwood, B.M. Oliver, S.M. Bruemmer, J. Nucl. Mater. 317 (2003) 32.
[14] D.J. Edwards, E.P. Simonen, S.M. Bruemmer, J. Nucl. Mater. 317 (2003) 13.
[15] Y. Dai, X. Jia, J.C. Chen, W.F. Sommer, M. Victoria, G.S. Bauer, J. Nucl. Mater. 296 (2001) 174.
[16] S.J. Zinkle, N. Hashimoto, D.T. Hoelzer, A.L. Quallas, T. Muroga, B.N. Singh, J. Nucl. Mater. 307–311 (2002) 192.
[17] M. Horiki, M. Kiritani, J. Nucl. Mater. 246 (1994) 212.
[18] S.M. Bruemmer, E.P. Simonen, P.M. Scott, P.L. Andresen, G.S. Was, J.L. Nelson, J. Nucl. Mater. 274 (1999) 299.
[19] G.S. Was, J.T. Busby, Philos. Mag. 85 (2005) 443.
[20] R. Stoenescu, Doctoral thesis 3326, EPFL, 2005.
[21] U. Stuhr, Nucl. Instrum. and Meth. A 545 (2005) 319.
[22] U. Stuhr, H. Spitzer, J. Egger, A. Hofer, P. Rasmussen, D. Graf, A. Bollhalder, M. Schild, G. Bauer, W. Wagner, Nucl. Instrum. and Meth. A 545 (2005) 30.
[23] D.J.H. Cockayne, I.L.F. Ray, M.J. Whelan, Philos. Mag. 20 (1969) 1265.
[24] M.L. Jenkins, M.A. Kirk, Characterisation of Radiation Damage by Transmission Electron Microscopy, Institute of Physics, Bristol and Philadelphia, 2001.
[25] J.H. Spence, J.M. Zuo, Electron Microdiffraction, Plenum, New York and London, 1992.
[26] P. Hirsch, A. Howie, R. Nicholson, D.W. Pashley, M.J. Whelan, Electron Microscopy of Thin Crystals, Robert E. Krieger Publishing Co Inc, 1977.
[27] K. Nakata, S. Ikeda, S. Hamada, A. Hishinuma, J. Nucl. Mater. 233–237 (1996) 192.
[28] H. Shaikh, G. George, F. Schneider, K. Mummert, H.S. Khatak, Mater. Corros. 51 (2000) 719.
[29] T. Nagasaka, N.J. Heo, T. Muroga, A. Nishimura, H. Watanabe, M. Narui, K. Shinozaki, J. Nucl. Mater. 329–333 (2004) 1539.
[30] P.A. Stadelmann, Ultramicroscopy 21 (1987) 131.
[31] R. Schäublin, Microsc. Res. Tech. 69 (5) (2006) 305.
[32] T.S. Byun, E.H. Lee, J.D. Hunn, J. Nucl. Mater. 321 (2003) 29.
[33] E.H. Lee, J.D. Hunn, T.S. Byun, L.K. Mansur, J. Nucl. Mater. 280 (2000) 18.
[34] E.H. Lee, J.D. Hunn, N. Hashimoto, L.K. Mansur, J. Nucl. Mater. 278 (2000) 266.
[35] N. Hashimoto, E. Wakai, J.P. Robertson, J. Nucl. Mater. 273 (1999) 95.
[36] R.E. Schramm, R.P. Reed, Metall. Trans. A 6 (1975) 1345.
[37] R. Schäublin, Z. Yao, N. Baluc, M. Victoria, Philos. Mag. 85 (2005) 769.
[38] S.J. Zinkle, J. Nucl. Mater. 150 (1987) 140.
[39] S.J. Zinkle, P.J. Maziasz, R.E. Stoller, J. Nucl. Mater. 206 (1993) 266.
[40] S.J. Zinkle, A. Horsewell, B.N. Singh, W.F. Sommer, J. Nucl. Mater. 212–215 (1994) 132.